Using digital pathology to analyze the murine cerebrovasculature

Dana M Niedowicz[1] (iD)**, Jenna L Gollihue[1], Erica M Weekman[2],
Panhavuth Phe[1], Donna M Wilcock[2], Christopher M Norris[1,3]
and Peter T Nelson[1,4]**

Abstract

Research on the cerebrovasculature may provide insights into brain health and disease. Immunohistochemical staining is one way to visualize blood vessels, and digital pathology has the potential to revolutionize the measurement of blood vessel parameters. These tools provide opportunities for translational mouse model research. However, mouse brain tissue presents a formidable set of technical challenges, including potentially high background staining and cross-reactivity of endogenous IgG. Formalin-fixed paraffin-embedded (FFPE) and fixed frozen sections, both of which are widely used, may require different methods. In this study, we optimized blood vessel staining in mouse brain tissue, testing both FFPE and frozen fixed sections. A panel of immunohistochemical blood vessel markers were tested (including CD31, CD34, collagen IV, DP71, and VWF), to evaluate their suitability for digital pathological analysis. Collagen IV provided the best immunostaining results in both FFPE and frozen fixed murine brain sections, with highly-specific staining of large and small blood vessels and low background staining. Subsequent analysis of collagen IV-stained sections showed region and sex-specific differences in vessel density and vessel wall thickness. We conclude that digital pathology provides a useful tool for relatively unbiased analysis of the murine cerebrovasculature, provided proper protein markers are used.

Keywords

Aperio ScanScope, arteriolosclerosis, immunohistochemistry, microvessel, VCID

Received 9 June 2023; Revised 18 October 2023; Accepted 23 October 2023

Introduction

Cerebrovascular pathology is associated with age-related neurologic diseases, including Alzheimer's disease, limbic predominant age-related TDP-43 encephalopathy with hippocampal sclerosis (LATE+HS), and stroke.[1–3] A wide range of pathological changes occur in small arterioles and capillaries- arteriolosclerosis, infarcts, and microbleeds have all been linked to dementia.[4–7] Additional age-related changes such as arterial stiffening, blood brain barrier breakdown, endothelial dysfunction, and reduced neurovascular coupling are also highly prevalent in human populations.[1,8,9]

Susceptibility to a variety of diseases, including many that are age-related, are known to be sexually dimorphic, and the disease trajectory and severity can vary between males and females.[10–13] Though sex difference in vascular structure and function exist throughout the lifespan, susceptibility to cardiovascular and cerebrovascular diseases increases substantially in post-menopausal females.[14–18] Because of this sex disparity, there is a renewed focus on sex as a variable in human studies, and use of both male and female mice is now required in studies funded by the U.S. National Institutes of Health (NIH).

An important part of investigations into the underlying mechanisms and potential therapeutics of many

[1]Sanders Brown Center on Aging, University of Kentucky, Lexington, KY, USA
[2]Stark Neurosciences Research Institute, Department of Neurology, Indiana University School of Medicine, Indianapolis, IN, USA
[3]Department of Pharmacology, University of Kentucky, Lexington, KY, USA
[4]Department of Pathology, University of Kentucky, Lexington, KY, USA

Corresponding author:
Dana M Niedowicz, 789 S. Limestone, Lee Todd Jr. Building, 5th Floor, Lexington, KY 40536, USA.
Email: dana.niedowicz@uky.edu

diseases is immunohistochemical (IHC) staining of various proteins, followed by qualitative and quantitative analyses of stained tissue. There are many potential blood vessel markers used routinely for IHC, though they can vary with respect to reactivity with large versus small blood vessels and many can show reactivity with other cell types. In addition, though there is overlap in the reactivity of some antibodies (i.e., they stain both human and rodent tissue), others show no cross-reactivity, making species-specific optimization of antibodies necessary. Nonspecific background staining is a known potential problem in mouse tissue, and reactivity of anti-mouse secondary antibodies with murine IgG can both obscure the desired staining and confuse analysis.[19] Therefore, it is essential to evaluate individual antibodies in the context of the desired evaluation (arteries, capillaries, etc.), and to optimize the protocol based on fixation method, section thickness, method of quantitation, etc.

Beyond the selection of antibodies and proteins for evaluation, changes in stain area as well as cell/tissue structure may be used to assess changes conferred by the genetic, environmental, or pharmaceutical manipulation. As a pre-eminent translational model in laboratory settings, rodents have been widely used to model these pathological processes. Adequately powered studies using rodents can involve dozens, or even hundreds, of mice, making single-slide visualization and analysis tedious and time-consuming. Further, there are shortcomings in the ability of the human eye to detect subtle histomorphological changes.[20,21] Therefore, a rigorous, quantitative, high-throughput method of cerebrovascular histomorphological assessment is desirable.

Digital pathology has been used extensively in both clinical and research settings to facilitate high throughput screening and analysis of human samples.[22–25] Among the advantages of digital pathology are the algorithm-driven analysis of digitized images, reducing bias and improving quantitation of various parameters.[26–28] In addition to measurements of staining intensity and coverage, some software packages can be used to analyze microvessels via algorithms that analyze metrics of blood vessel geometry (which may track with healthy or disease states), such as blood vessel lumen area and wall thickness.[22,29,30] When using algorithm-based quantitation, it is essential to optimize the immunoreactivity's signal-to-noise ratio, as high background staining may prevent accurate discrimination of blood vessels versus other histological features.

In this study, we tested both formalin-fixed paraffin embedded (FFPE) and frozen-fixed mouse brain sections with a variety of antibodies directed at blood vessel/neurovascular unit proteins. We asked which

marker was the most effective for specific staining of the murine cerebrovasculature. We also explored the impact of various technical parameters, with the specific intent to perform high-throughput digital pathology.

Materials and methods

Mice

Mice were obtained from commercial sources (The Jackson Laboratory, National Institute on Aging) or in-house breeding colonies at the University of Kentucky. Mice were fed and watered *ad libitum*, and maintained on a constant light: dark cycle (14:10). Mice were euthanized by barbiturate overdose (Beuthanasia, Fatal Plus, or similar: Covetrus, Lexington, KY), followed by transcardial perfusion with phosphate buffered saline (PBS). Mice used for the sex and region-specific analyses were C57Bl/6J mice (N = 6/sex) fed a standard rodent chow (BioServ, Flemington, NJ), and euthanized at 18 months old. All animal work was conducted with prior approval from the University of Kentucky Institutional Care and Use Committee and performed in accordance with U.S. Public Health Service Policy on Humane Care and Use of Laboratory Animals.

FFPE tissue processing

Brains were fixed in 10% phosphate-buffered formalin for at least 24 hours before processing (Tissue Tek VIP). The processing program used increasing concentrations of ethanol for 30 minutes each (70-100%), followed by 45 minutes in 100% ethanol, 30 minutes in 1:1 ethanol/xylene, and two 30-minute steps in 100% xylene. Processing was completed with four cycles in 60 °C paraffin (1 X 5 minutes, 3 X 15 minutes). Brains were embedded in paraffin and sectioned to eight micron thickness using a microtome. Slide-mounted sections were deparaffinized by sequential submersion in xylene followed by decreasing concentrations of ethanol. For heat-mediated antigen retrieval, slides were boiled in buffer (pH 6 or pH 9) for six minutes. Endogenous peroxidases were neutralized with 3% H_2O_2 (30 minutes, room temperature), followed by blocking in normal serum from the secondary antibody host species (15% horse serum, 5% goat serum, 5% rabbit serum in Tris-buffered saline (TBS)), 1 hr., room temperature). For pepsin-mediated retrieval, sections were first treated with 3% H_2O_2 (30 minutes, room temperature), then incubated with pepsin (20 minutes, 37 °C), and blocked in 5% normal goat serum (1 hour, room temperature). Sections were incubated overnight at 4 °C with primary antibody diluted

in TBS with normal serum (for list of the antibodies used, see Table 1). After washing, slides were incubated with either biotinylated horse anti-mouse, biotinylated rabbit anti-rat, or biotinylated goat anti-rabbit secondary antibody (Vector Laboratories, Burlingame, CA: 1 hour, room temperature), followed by ABC reagent (Vector Laboratories: 1 hour, room temperature). Slides were developed with DAB (Dako/Agilent, Santa Clara, CA), counterstained with hematoxylin (Vector Laboratories), dehydrated, and cover slipped with toluene-based mounting media (Fisher Scientific, Hampton, NH).

Frozen fixed tissue processing

For collagen IV and DP71 staining, brains were post-fixed in 4% paraformaldehyde for 24 hours, then submerged in 20% sucrose until sunk to the bottom of the tube (at least 24 hours). For CD31, brains were submerged sequentially in 10, 20, and 30% sucrose (24 hours each). Brains were sectioned in the coronal or horizontal plane to 25–40 μm thickness using a freezing, sliding microtome (American Optical AO 860). Free floating sections were either placed in cryopreservative (25% glycerol, 25% ethylene glycol in 1X phosphate-buffered saline (PBS) and stored at $-20°C$ (collagen IV and DP71) or stored in 1X PBS with azide at $4°C$ (CD31) until immunostaining was performed. The conditions for each antibody are below:

1. *CD31*: Heat-mediated antigen retrieval was performed with a citrate-based buffer (pH 6, 95°C, 12 min.), followed by formic acid (70%, 3 min.). Endogenous peroxides were neutralized with 3% hydrogen peroxide (H_2O_2, 70% methanol) for 15 minutes. Sections were washed in PBS with 4% goat serum. Sections were blocked with 5% goat serum (in PBS with 0.1% Triton X-100 and 0.019% L-lysine) for one hour. The primary antibody was diluted 1:1000 in 4% goat serum.

2. *Collagen IV*: Endogenous peroxidases were neutralized with 3% H_2O_2 (90% methanol for 30 minutes. Heat-mediated antigen retrieval was performed using a Tris-based buffer (pH 9; 20 minutes, 80°C) and washed in TBS (with 0.1% Triton X-100 and 3% BSA). Sections were then blocked with 5% goat serum in TBS (with 0.1% Triton X-100 and 3% BSA) for 1 hour at room temperature. The primary antibody was diluted 1:1000 in blocking buffer.

3. *DP71*: No antigen retrieval was performed for this antibody. Endogenous peroxidases were neutralized with 3% H_2O_2 (10% methanol) for 15 minutes. Sections were washed in PBS with 4% goat serum, then blocked in 4% goat serum (in PBS with 0.2% Triton X-100 and 0.019% L-lysine) for 30 minutes. The primary antibody was diluted 1:1000 in 4% goat serum.

All sections were incubated overnight with the desired primary antibody (4°C). After washing, sections were incubated with the goat anti-rabbit secondary antibody (2 hours, room temperature), followed by ABC reagent (1 hour, room temperature). DAB was used as the HRP substrate (Vector Labs). No counterstain was used. Sections were mounted onto slides and dried overnight, before dehydration and the addition of DPX mounting medium and a coverslip.

Slide scanning and analysis

Slides were scanned using an Aperio ScanScope AT2 (Leica Biosystems, Deer Park, IL) at 40X magnification and the resulting virtual slide stored on a dedicated server. eSlides were analyzed using the Aperio Microvessel Analysis Algorithm, part of the Image Analysis software. This analysis algorithm uses color deconvolution, and is tuned to differentiate between dark-brown DAB staining and unstained or counterstained background. Pixels with DAB's color profile are segmented from the rest of the image, and light/

Table 1. Antibodies tested for microvessel staining.

Target protein	Company	Catalog #	Host species	Dilution (FFPE)	Dilution (free floating)
CD31	Abcam	ab281583	Rabbit	1:2000	1:1000
CD34	Dako	QBEnd10	Mouse	1:2	n/a
	Abcam	ab8158	Rat	1:100	n/a
	Abcam	ab81289	Rabbit	1:2500	n/a
	Thermo	14-0341-02 (RAM34)	Rat	1:50	n/a
	Thermo	PA5-89536	Rabbit	1:50	n/a
	Thermo	MA5-29674	Rabbit	1:5000	n/a
Collagen IV	Abcam	ab236640	Rabbit	1:1000	1:1000
Dystrophin (DP71)	Abcam	ab15277	Rabbit	1:500	1:1000
VWF / Factor VIII	Abcam	ab287962	Rabbit	1:50	n/a

dark thresholding allows for noise reduction by eliminating background, non-vessel pixels from the deconvoluted image.[31,32] Remaining vessels and vessel fragments are joined by the algorithm based on their distance from each other to assemble a completed vessel, from which morphometric data is produced. The default settings were used for analysis, except for the light and dark thresholds, which were adjusted for each slide to capture the vessels while excluding non-specific background staining as much as possible. Regions of interest (ROI) were drawn separately around the hippocampus and cortex for each slide, and the microvessel parameters (vessel number, perimeter, lumen, wall thickness, etc.) calculated for each ROI.

Statistics

All animal data from this study are reported according to AARIVE 2.0 guidelines.[33] For assessment of antibody efficacy in digital pathology, a single section for each condition was scanned and analyzed. In order to determine the effect of sex on microvessel parameters, each mouse's data were counted individually, then used to calculate group averages (N = 6/group). Data are reported as group mean ± standard deviation. Data were analyzed for statistical significance with SPSS (Hewlett Packard; Palo Alto, CA). Data sets were first evaluated using the Shapiro-Wilk test for normality. Normally-distributed data were analyzed using the general linear model (GLM) module for ANOVA with sex or brain region as the independent variable. For explanation of this model, using two-tailed statistical tests:

https://www.ibm.com/support/knowledgecenter/SSLVMB_25.0.0/statistics_mainhelp_ddita/spss/advanced/idh_glm_multivariate.html

Post hoc analyses were performed as a Tukey's HSD or Bonferroni correction. Data that were not normally distributed were analyzed using a Mann-Whitney U test for non-parametric data. The p-values for normality testing are listed in the figure legend. The p-values for significance testing are shown on the relevant graphs.

Results

The workflow is shown in Figure 1. Briefly, mouse brain sections were stained for different blood vessel markers, then scanned into the Aperio ScanScope AT2 in order to obtain a digital image (Figure 1(a)). For each image, the microvessel algorithm was applied after titrating the dark and light thresholds to prevent detection of non-vessel objects while maximizing the number of vessels detected. The microvessel algorithm

outputs several different parameters, including vessel perimeter, lumen area, and wall thickness. The markers selected stain a variety of blood vessel-related structures, including astrocyte endfeet (DP71), lamina (collagen IV), and endothelial cells (Figure 1(b)). A typical micrograph stained for blood vessel markers is shown in Figure 1(c), along with a false color markup, illustrating the shading used to denote lumen versus vessel wall.
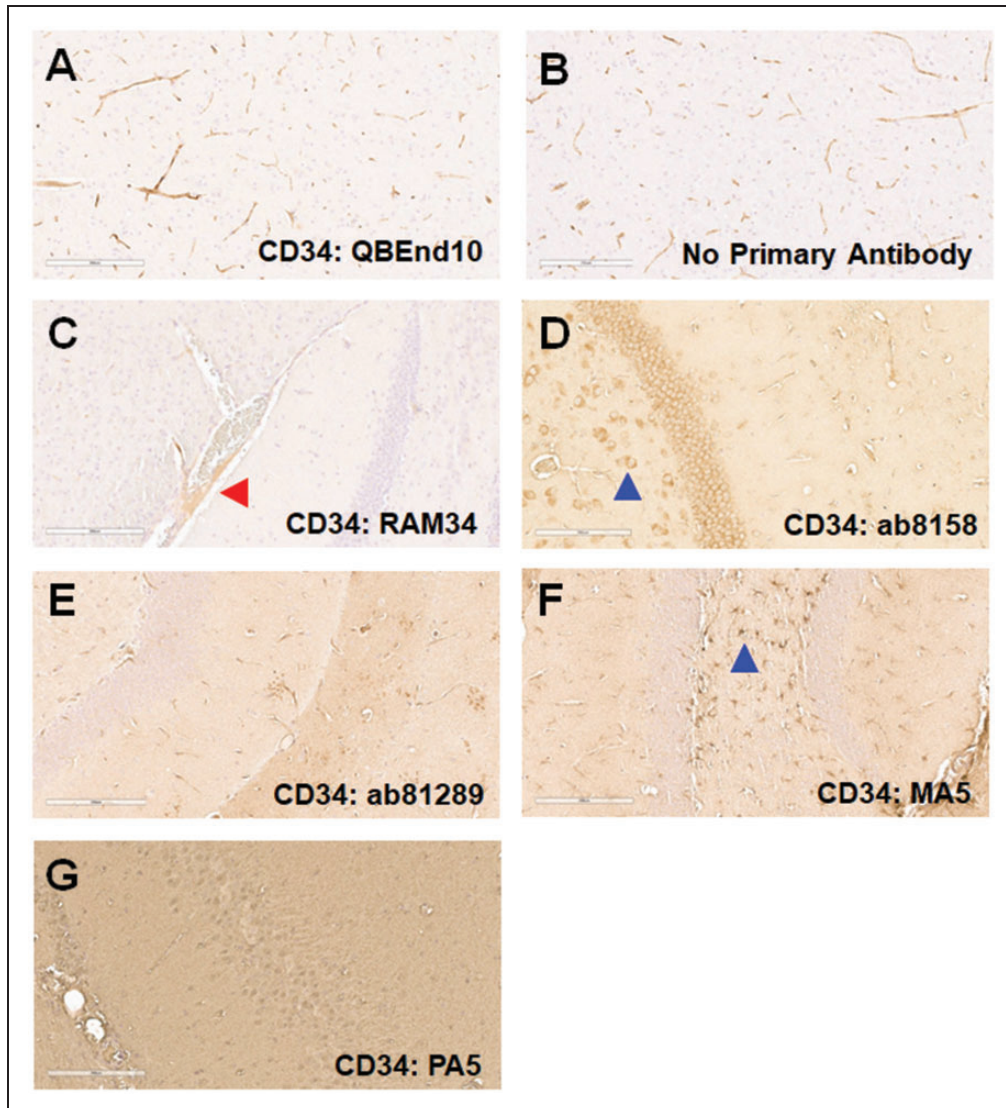
FFPE staining

CD34. We previously showed that CD34 staining of human FFPE brain sections is optimal for microvessel analyses.[22] We therefore investigated whether CD34 would also be a good marker for the murine cerebrovasculature. We first tested QBEnd10, which we had successfully used to stain human brain microvessels. Though there was apparent microvessel staining with this antibody (Figure 2(a)), a similar pattern was seen when the primary antibody was omitted; therefore, this staining was likely attributable to non-specific binding of the anti-mouse IgG secondary antibody (Figure 2(b)). We next tested several additional anti-CD34 antibodies, focusing on those generated in rabbit and rat in order to prevent this non-specific binding to murine blood vessels. RAM34 (Figure 2(c)) displayed some immunostaining, albeit light, of blood vessels, but this was limited to larger arteries and arterioles (red arrow). Antibodies ab8158 (Figure 2(d)) and ab81289 (Figure 2(e)) showed limited reactivity with small blood vessels, but also reacted with cells such as neurons (blue arrows). MA5-29674 (Figure 2(f)) reacted with astrocytes (blue arrow), but not blood vessels, whereas PA5-89536 (Figure 2(g)) showed high background in our hands, without any staining of cells or vessel structures.

Additional Candidate Markers. As we were not able to identify a viable anti-CD34 antibody to use with mouse tissue, we explored other small blood vessel markers in FFPE. Slides stained for CD31 (Figure 3(a)) displayed moderate background staining and some staining of blood vessels. Slides stained for collagen IV showed very low background and moderate staining of large and small blood vessels (Figure 3(c)). DP71 localizes to astrocyte endfeet.[34,35] Because endfeet directly contact blood vessels, DP71 can be used as a protein marker for visualization.[36] Anti-DP71 (Figure 3(e)) showed moderate vessel staining, but also had a moderately high background, including staining of cell bodies. Anti-von Willebrand Factor (VWF) led to very high background, with no obvious blood vessel staining (Figure 3(g)). The slides were next analyzed using the Aperio microvessel algorithm. Though some anti-CD31-stained vessels were detected
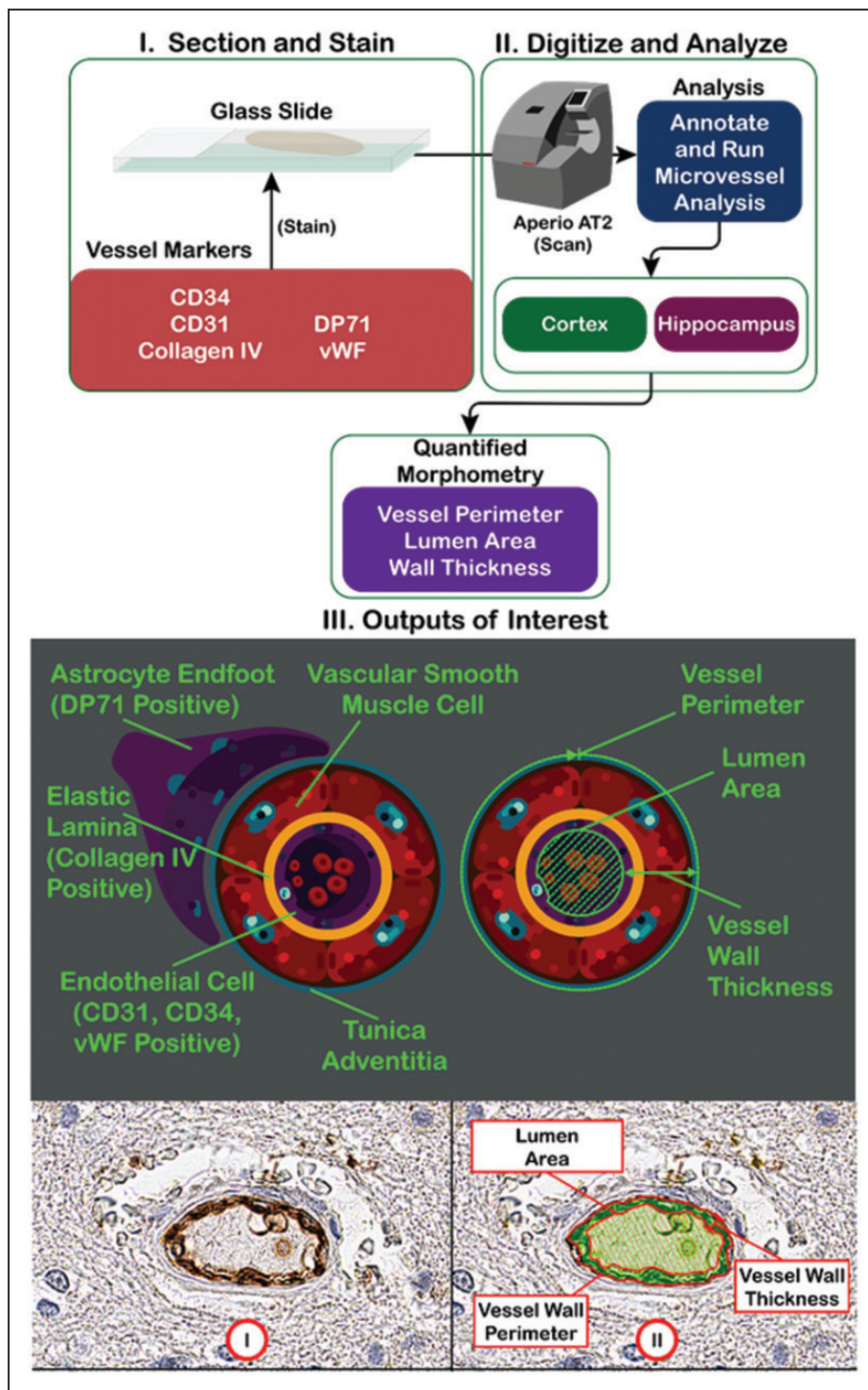
Figure 1. Digital pathology workflow. (*Upper Panel*) FFPE (on slides) or frozen-fixed (free floating) mouse brain sections were stained for a variety of blood vessel markers. The resulting slides were scanned by the Aperio ScanScope AT2 slide scanner to obtain digitized images. Two regions of interest (cortex and hippocampus), were outlined, then analyzed, using the supplied microvessel algorithm to quantify different vessel parameters, such as vessel density, vessel perimeter, lumen area, and vessel wall thickness. (*Middle Panel*) I. The blood vessel markers used are specific for a variety of blood vessel structures, including astrocyte endfeet (DP71), elastic lamina (collagen IV), and endothelial cells (CD31, CD34, and von Willebrand Factor). *II.* A representation of the output measurements in relation to the blood vessel structure. (*Lower Panel*) I. A representative micrograph with a DAB-stained blood vessel. II. A false color markup of the vessel by the microvessel algorithm, showing the relevant output parameters.

Figure 2. CD34 staining. Mouse brain sections were stained for CD34 using a variety of antibodies. (a) While QBEnd10 staining showed blood vessel staining, this was indistinguishable to that seen in the negative, anti-mouse secondary antibody control. We next evaluated anti-CD34 antibodies not generated in mouse (b). RAM34 stained only very large blood vessels (red arrow), albeit very lightly (c). ab8158 showed very light, inconsistent blood vessel staining, but also significant staining of neuronal cells (blue arrow: d). ab81289 showed light, inconsistent blood vessel staining, but with moderate background staining (e). MA5-29674 predominantly stained glial cells (blue arrow), but did not stain blood vessels (f). PA5-89536 showed no staining, other than a very high background (g).

by the algorithm, there were many visible vessels that were not detected (red arrow, Figure 3(b)) and other areas where "vessels" were detected that did not exist (blue arrows). There was very low background in the slide stained with anti-collagen IV, but due to the light staining, very few vessels were detected by the algorithm (Figure 3(d)). There was good detection of vessels in the DP71-stained slide, but many neuronal cells were also detected (Figure 3(f)). The background was so high in the slide stained for VWF, that few vessels were detected and the majority of the analyzed area was excluded completely by the algorithm (Figure

3(h)). The numbers of detected vessels (Figure 3(i)) and vessel density (Figure 3(j)) were much higher for CD31 and DP71 stained hippocampus and cortex than either collagen IV or VWF, likely due to the counting of stained cells and background areas (blue arrows).

Collagen IV optimization. Though in our preliminary experiments there were relatively few vessels detected due to light staining, collagen IV gave the best combination of low background and blood vessel-specific staining. Therefore, we sought to optimize the
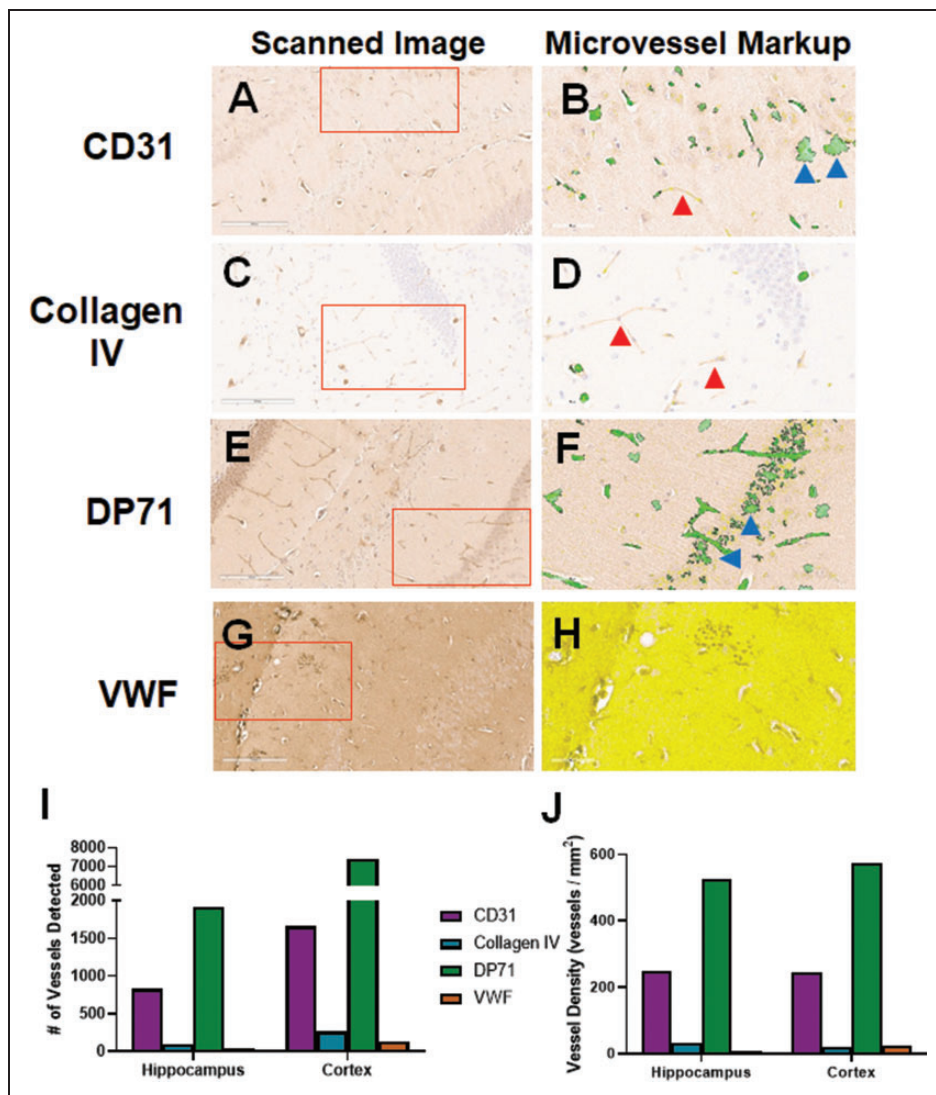
Figure 3. Initial evaluation of non-CD34 blood vessel markers. We tested a variety of potential blood vessel markers for use in mouse brain tissue. (a) CD31 stained blood vessels lightly, but also showed some non-vascular cell staining. (b) Analysis by the microvessel algorithm identified blood vessels, but also cell staining (blue arrows). There were many vessels left unidentified (red arrow). (c) Collagen IV stained blood vessels lightly, with very low background. (d) Given the light staining, the microvessel algorithm clearly missed some visible blood vessels (red arrows). (e) The DP71 stained slide had moderately high background staining, but showed both blood vessel and cell body staining. (f) The microvessel algorithm readily detected blood vessels, but also misidentified cell staining as blood vessels (blue arrows). (g) The von Willebrand Factor (VWF) stained slide had very high background. (h) The background was so high that the algorithm could not identify any blood vessels. The entirety of the displayed region of interest was excluded from analysis (yellow shading). The number of vessels identified by the algorithm (i), as well as the vessel density (j) varies significantly for each antibody. CD31 and DP71 identified the most vessels, possibly due to the non-vessel cell staining. Red boxes indicate the region of interest analyzed by the microvessel algorithm, shown in the second panel for each antibody.

collagen IV-positive staining by utilizing a variety of antigen retrieval methods. Our original tests of this antibody used a heat-mediated, pH 6 antigen retrieval (Figure 4(a)). We tried a pH 9 solution for heat-mediated retrieval but this led to a similar level of blood vessel staining than the lower pH (Figure 4(c)). We next tested the ability of enzyme-mediated retrieval to enhance blood vessel staining using anti-collagen IV. Pepsin treatment for 10 minutes increased

blood vessel staining (Figure 4(e)), compared with heat-mediated retrieval, while 20 minutes led to even more robust staining (Figure 4(g)). Downstream digital image analysis by the microvessel algorithm showed that all tested antigen retrieval methods yielded staining with very little background staining. However, there were many vessels that were undetected by the digital image analyses, though visible to the human eye, in the pH 6 (red arrows: Figure 4
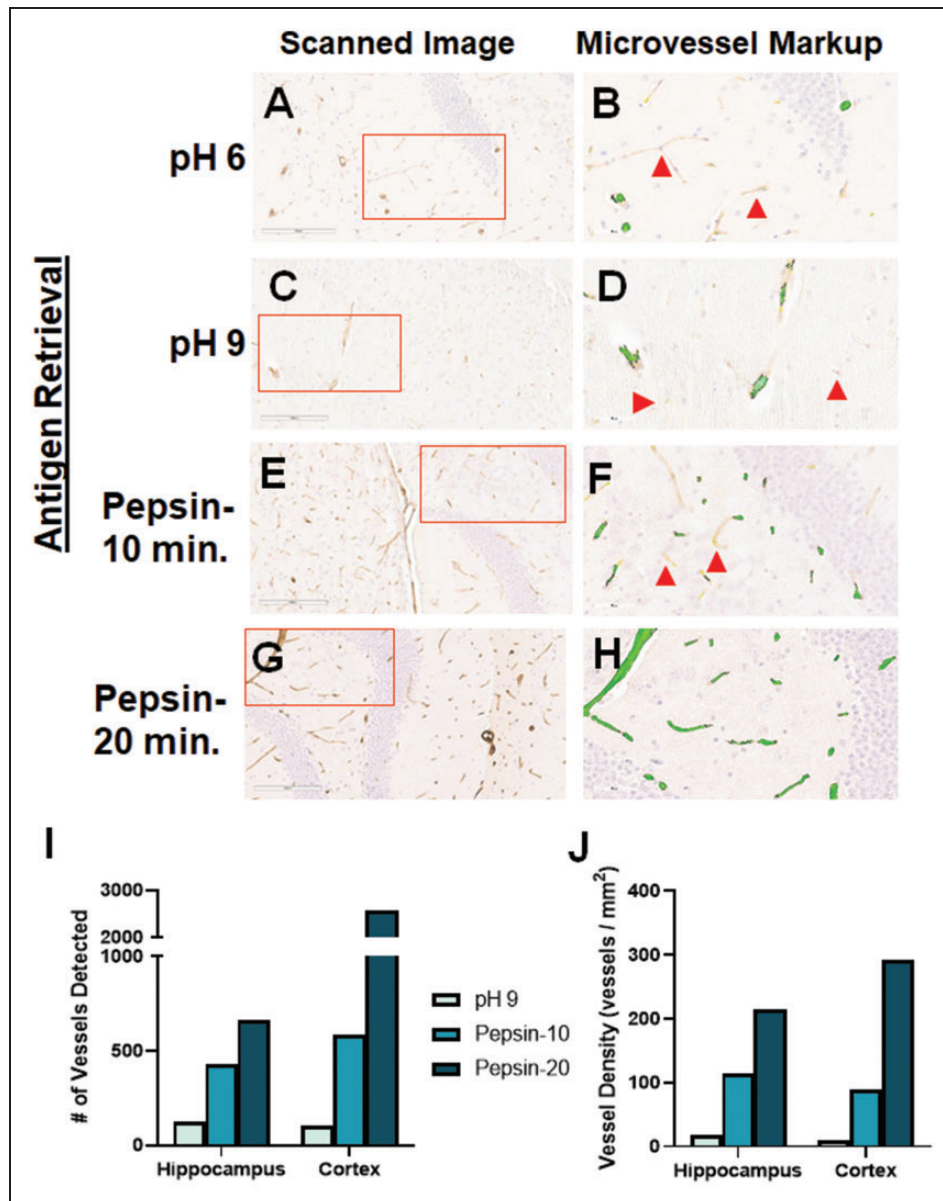
Figure 4. Optimization of collagen IV staining. We tested different antigen retrieval methods to improve the staining of blood vessels with anti-collagen IV. (a) Low pH heat-mediated antigen retrieval of collagen IV staining led to only light reactivity. (c) High pH heat-mediated antigen retrieval did not improve blood vessel staining. (b, d) Though the microvessel algorithm did detect some vessels, there were many lightly-stained vessels that were not identified (red arrows). (e) Pepsin-mediated retrieval for 10 minutes improved blood vessel staining, while maintaining a very low background. (f) The microvessel algorithm detected more vessels using this method, but still missed some that were lightly stained (red arrows). (g) Pepsin-mediated retrieval for 20 minutes further improved staining of blood vessels, both small and large, while retaining the low background. (h) The microvessel algorithm was able to detect all stained vessels in the region of interest, while minimizing detection of non-vessels. Each of the antigen retrieval methods tested yielded an increase in the number of vessels detected by the algorithm (i), as well as the vessel density (j). Red boxes indicate the region of interest analyzed by the microvessel algorithm, shown in the second panel for each antibody.

(b)), pH 9 (Figure 4(d)) and ten minutes of pepsin treatment (Figure 4(f)). Extending the pepsin treatment to 20 minutes led to detection of all blood vessels seen in the region of interest (Figure 4(h)), including both capillaries and arterioles. This result was evident whether looking at the number of blood vessels detected (Figure 4(i)), or the vessel density (Figure 4(j)).

Free floating sections

Staining of FFPE presents several challenges, including a potential increase in masking (decrease of staining) of antigens that reduces binding of antibodies. As such, it is common practice to stain frozen-fixed sections that have not been paraffin-embedded. Because these
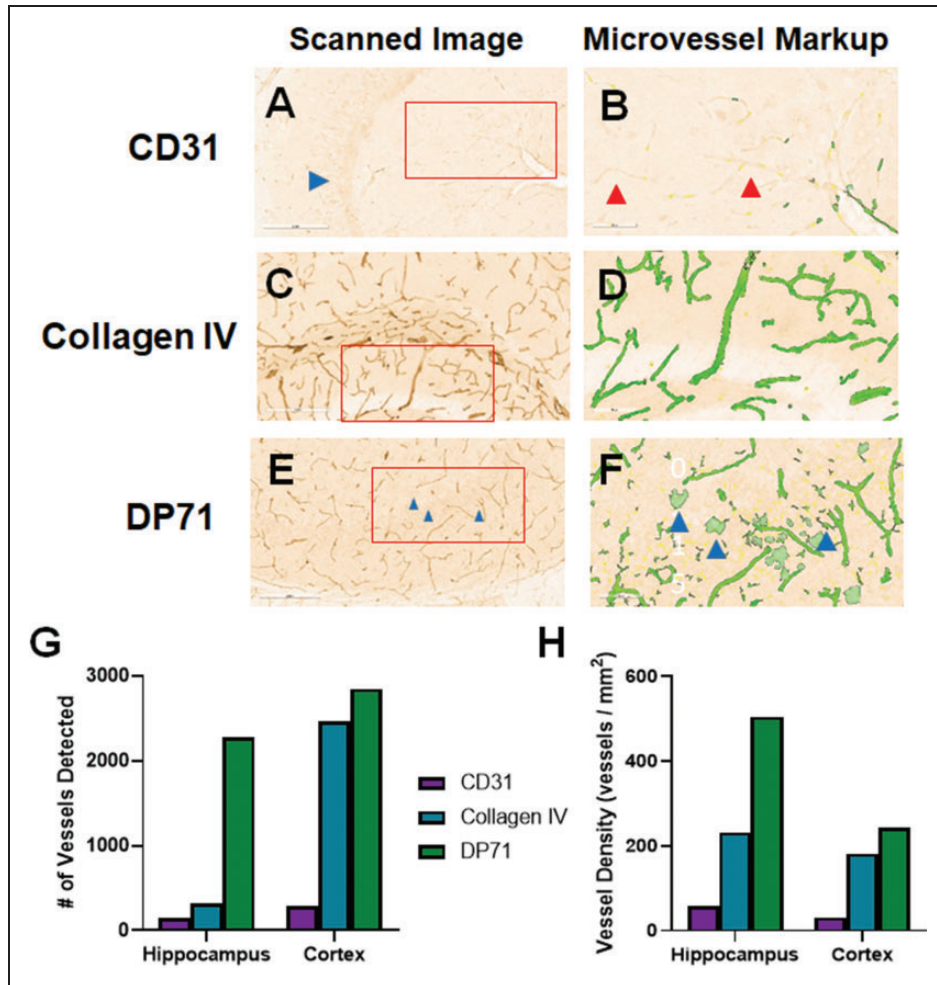
Figure 5. Staining for blood vessels in free-floating sections. We tested a few different blood vessel markers to determine whether they also work for frozen fixed brain sections. (a) CD31 showed light-inconsistent staining of blood vessels, but also stained cells in the dentate gyrus (blue arrow). (b) The microvessel algorithm detected a few blood vessels, but clearly missed some that were lightly stained (red arrows). (c) Collage IV robustly stained large and small blood vessels in both the hippocampus and cortex, which were readily detected by the microvessel algorithm (d). (e) DP71 also stained the blood vessels well, though there was apparent staining of astrocyte cells as well, which were erroneously identified as blood vessels by the microvessel algorithm (blue arrows; f). The algorithm identified more vessels in the DP71 stained slide than the other antibodies, likely due counting non-vessel stained cells (g), yielding a higher apparent blood vessel density (h). Red boxes indicate the region of interest analyzed by the microvessel algorithm, shown in the second panel for each antibody.

sections are often stained while free floating in solution, the techniques used can be quite different, especially with respect to antigen retrieval methods. We therefore tested three of the blood vessel markers that gave the best results in FFPE. Slides stained for CD31 showed some staining of blood vessels, though the signal-to-noise ratio was very low, as well as staining of neuronal cells in the dentate gyrus (blue arrow; Figure 5(a)). Collagen IV robustly stained large and small blood vessels in free floating mouse brain sections with relatively low background, even using heat-mediated antigen retrieval (Figure 5(c)). We attempted to use enzyme-mediated antigen retrieval for free-floating tissue, but the sections were robustly digested by the enzyme and not usable (*data not shown*). DP71 strongly stained blood vessels, though it also picked up cell bodies, such as astrocytes (Figure 5(e)). Analysis of these slides, using the microvessel algorithm, showed that CD31 staining led to very low detection by the algorithm (Figure 5(b)). Similar to FFPE, collagen IV staining of blood vessels lead to robust identification by the algorithm (Figure 5(d)). Many microvessels were detected in the DP71-stained slide as well (Figure 5(f)), though the astrocyte cell body staining was also mis-labeled as blood vessels by

the digital algorithm (blue arrows), leading to incorrect overestimation of blood vessel numbers. This was particularly problematic in the hippocampus, where the estimated vessel number was seven-fold increased versus that of the collagen IV-stained tissue section (Figure 5(g)). In addition, vessel density was much higher in the hippocampus than for the other stains (Figure 5(h)).

Choosing a preferred method to analyze the effect of sex on murine microvessel parameters

Given the observed staining results, the best candidate for microvessel staining of the murine cerebrovasculature was collagen IV, both for FFPE and free-floating sections. Using both preparatory techniques, there was a strong DAB signal, relative to the background, which is essential for accurate identification of the blood vessels. We next used this stain to test whether sex differences could be detected in the murine cerebrovasculature in middle-aged (18 months old) mice. We used FFPE sections because it was more convenient and used less antibody. With this approach, there was strong staining of microvessels in both the hippocampus and the cortex, with very low background (Figure 6(a) to (d)). Analyses using the microvessel algorithm showed differences between brain regions as well as sex differences in some of the measurements. There was no significant sex-specific difference in vessel density in the hippocampus or cortex (Figure 6(e)). Vessel density was greater in the cortex than the hippocampus in females ($p = 0.002$), though there was no difference between regions in the males. There was no sex- or region-specific difference in vessel perimeter in these animals (Figure 6(f)). Though it did not reach significance, there was a trend towards a larger lumen size in male versus female mice in the hippocampus ($p = 0.065$; Figure 6(g)). On the other hand, vessel walls were thinner in male than female mice in the hippocampus (mean difference 0.227 μm; $p = 0.048$; 95% CI [0.003–0.5; Figure 6(h)] and cortex (mean difference 0.185 μm; $p = 0.032$; 95% CI [0.019–0.351]). Vessel walls were also slightly thinner in the cortex of female mice, compared with hippocampal blood vessels (mean difference 0.143 μm; $p = 0.043$; 95% CI [0.006–0.281]).

Discussion

In this report, we optimized technical parameters for digital quantification of microvessel morphology in the murine brain. Unlike our studies of the human brain, we found that collagen IV IHC gave a desirable combination of technical features. Using collagen IV IHC, we were able to detect statistically significant differences in male and female mice in terms of cerebral vascular parameters.

The significance of the current study relates to five basic factors: 1. We evaluated a panel of various blood vessel markers, several antibodies, and tissue preparation conditions for murine brains, with an eye towards staining specificity and optimal signal-to-noise, 2. To our surprise, some of the "canonical" methods were not optimal, or even necessarily feasible, in our hands, 3. In the wake of a relatively unbiased approach to methods development, a data-driven, optimized IHC protocol was generated for morphometric assessment of microvessels in both FFPE and free-floating sections, 4. The optimized methodology was specifically oriented toward pairing with "downstream" digital pathologic assessments, and 5. These methods were applied, including in silico analyses, and we confirmed the potential for identifying differences between biological groupings. Ultimately, it is hoped that these methods can have a broad range of uses in the research field, particularly focused on how perturbations in murine biology correlate with small blood vessel morphometry in the brain.

Digital pathology provides opportunities for rigorous assessments of histomorphology, but the experimental methods requires technical optimization. Immunohistochemistry is a widely-used technique in both clinical and lab settings. However, an optimal signal: noise ratio of the stain itself is crucial for accurate downstream quantitation and analyses of the data. Achieving dependable results when studying mouse microvessel parameters requires identification of antibodies that specifically recognize blood vessels in the mouse brain, as well as optimization and validation of the procedure.

Though we and others have successfully used CD34 IHC as a microvasculature marker in human brain tissue,[22,37] our results indicated that this technical approach does not work as well in mouse brain tissue. We tried CD34 antibodies generated in three different animals (mouse, rat, and rabbit) and saw very sparse and inconsistent microvessel-specific staining (Figure 2). The mouse-generated antibody that we tested (QBEnd10) presented an additional problem in that the anti-mouse secondary antibody bound to endogenous murine IgG. (Figure 2(b)). Unfortunately, the non-specific binding with murine IgG was patchy and sparse and not appropriate for optimal digital pathologic downstream analyses.

There are several proteins/antigens that have been used via IHC to stain the vasculature, each targeting a distinct subset of cell types (Figure 1). We examined several of the most common blood vessel markers, with mixed results. The most common problem that
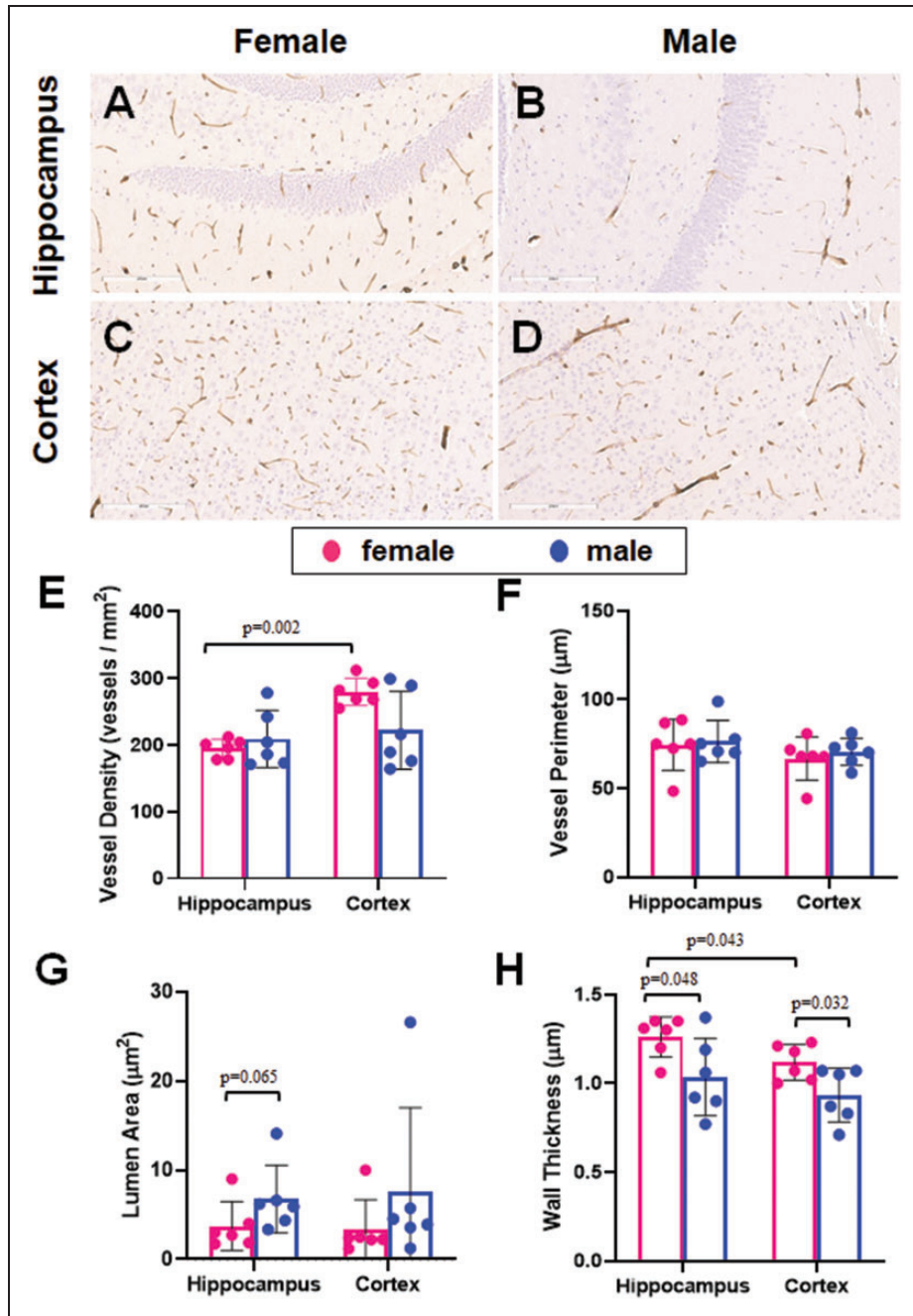
Figure 6. The effect of sex on cerebral microvessels. FFPE sections of mouse brain were stained for microvessels using collagen IV as a marker. Each slide was subsequently scanned using the Aperio ScanScope and analyzed using the microvessel algorithm feature of the associated ImageScope software, drawing regions of interest around the hippocampus and cortex of each section. Representative images for each brain region are shown for both female (a, c) and male (b, d) mice. (e) Vessel density was similar in males and females in the hippocampus, while females had a higher density in the cortex. (f) Vessel perimeter was not significantly different between females and males in either brain region tested. (g) The lumen area trended larger in the males than the females in the hippocampus. (h) Wall thickness was slightly thinner in males compared with females in both brain regions. Vessel walls were thicker in the hippocampus than the cortex of female mice. $N = 6$/sex. The distribution of data was evaluated by a Shapiro-Wilk test for normality (e, $p = 0.017$, f, $p = 0.23$, g, $p < 0.0001$, h, $p = 0.425$). Vessel density and lumen are were subsequently analyzed with a Mann-Whitney U test for nonparametric data. Vessel perimeter and wall thickness were subsequently analyzed by ANOVA.

we observed was high background relative to the vascular staining. This issue would make it difficult for a subsequent computational algorithm to differentiate between background and vessel, skewing identification of vessels and calculation of their various characteristics. Other antibodies, particularly that for DP71, showed non-vascular cell staining in addition to vascular staining, i.e. lack of specificity, which would similarly lead to inaccurate quantitation.

In our hands, collagen IV IHC gave the cleanest signal, coupled with very low background (Figure 3(c)). Optimization of the collagen IV antibody in FFPE revealed that pepsin-mediated antigen retrieval led to more robust staining of blood vessels than heat-mediated retrieval using different pH (Figure 4(a), (c), (e) and (g)). Because collagen IV is a marker of the vessel lamina, the antibody used here stains the luminal portion of both small and large blood vessels. In order to achieve a more complete picture of vascular changes, it would be ideal to be able to use complementary markers of a variety of cell and structure types (e.g. endothelial, smooth muscle, pericytes, astrocytic endfeet, lamina, etc.), as some pathologies presumably affect some cell types and/or microdomains more than others. Such a comprehensive analysis will require identification of appropriate reagents for the additional cell types, however.

Though FFPE may be a good option for IHC experiments, due to long-term stability of the paraffin blocks and suitability for thin sections, using frozen fixed sections may confer some advantages. For instance, the processing that occurs prior to embedding in paraffin may effectively "mask" some epitopes, leading to inconsistent staining.[38–40] In addition, some epitopes are known to be labile and are effectively lost during the harsh FFPE processing steps.[41,42] Furthermore, the equipment needed for processing and embedding are specialized and may not be readily available. On the other hand, frozen fixed sections are often 3-5 times thicker than FFPE sections, which can impact the ability of the antibody to penetrate into the tissue. Additionally, free floating sections are more delicate due to the absence of a stabilizing matrix, such as a glass slide, requiring gentle handling and antigen retrieval. With this in mind, we examined several blood vessel markers in frozen fixed mouse brain tissue. Though the background tended to be higher overall in these sections, the antibody against collagen IV led to robust staining of blood vessels (similar to the results with FFPE murine brains) that easily stood out against the background (Figure 5(c)). despite a less stringent antigen retrieval method (pH 9 at 80 °C vs. pepsin).

The use of anti-collagen IV antibodies to stain blood vessels is not new, but published protocols vary.[43–45]

Some previous published reports used heat-mediated antigen retrieval at both low and high pH,[46,47] but these approaches did not lead to robust staining of mouse brain microvessels in our hands. Other describe successful collagen IV immunostaining with pepsin-mediated retrieval,[48,49] even with free-floating sections. In our studies of mouse brain, we found that the free-floating sections were substantially digested by the pepsin treatment and this approach was not practical in this context.

Despite their importance to pre-clinical research, there have been relatively few studies that have rigorously reported on murine cerebral microvessel morphometrics using IHC experiments. Even fewer prior published studies assessed the technical results of different approaches. By contrast, as number of prior published studies have used various radiological and intravital methods (for examples, see[50–56]). We feel that neuropathologic observations are an important complement to other modalities, as a time-honored source of insights into healthy and disease states.

Many of the prior studies of mouse brain pathologic specimens have focused on neurodegenerative diseases, brain tumors, and brain trauma.[22,44,45,57–59] These studies have applied various methodologies, including estimation-based quantification methods such as fractal analysis[60,61] and stereology.[62–64] Other computational methods have been investigated; Mozumder and colleagues captured histological images of microvessels in sectioned tissue to estimate capillary morphometrics via digitally-reconstructed 2 D models.[65] Similarly, Freitas-Andrade published a protocol for analyzing cerebrovascular microvessels in a relatively unbiased manner, using immunofluorescence with subsequent 3 D digital reconstruction.[66] Further, several studies have employed image segmentation software to analyze vessel morphometry directly.[57,67,68] Despite progress in the field, our study underscores that there remains a need for technical studies so that different investigators can ask a range of questions with tools that are optimized and, perhaps in the future, standardized.

There are some caveats and limitations to using the microvessel algorithm to quantify vessel number and characteristics. For instance, there are some measurements that are not calculated that could be of interest: diameter and length, for instance. More broadly, the image obtained is two dimensional, which may limit appreciation of the three-dimensional aspects of the vasculature, thus requiring additional software applications. This may also lead to overestimation of vessel number, since a single thin section may not detect the connection between vessels when the connections are out of plane. In addition, it is important when using digital pathology to carefully adjust thresholds so that

vessels are delineated from background. It is also important to compare vessel parameters from similar brain regions- vessel sizes, orientation (e.g., anterior-posterior vs dorsal-ventral) wall thickness, etc. can vary significantly within and between different structures. There appears to be more variation in some of the estimated parameters than others, particularly lumen area (Figure 6(g)). This may be due to difficulties of the algorithm to estimate lumen based solely on variations in shading, but also highlights the importance of comparing consistently stained slides and to carefully titrate the algorithm staining thresholds Despite the difference in the processing and staining protocols of the FFPE versus free floating sections, microvessel analysis yielded the detection of roughly the same density of vessels, particularly in the hippocampus when anti-collagen IV was used (Figure 4(j) and 5(h)).

Effect of brain region and sex. Vessel density in hippocampus and cortex was similar in male and female mice brains (Figure 6(e)). However, the observed vessels in males had thinner vessel walls in both brain regions studied, as well as a trend towards larger lumen area in the hippocampus (Figure 6(g) and (h)). This could be indicative of sex-dependent differences in vascular biology, which may have implications for cerebral blood flow, hemodynamics, neurovascular coupling, or other aspects of cerebrovascular health in middle aged mice.[17,46,69–71] Whether the measured differences translate to hemodynamic differences in these mice is currently unknown. In prior published studies of young mice, as well as humans, females have been shown to have higher cerebral blood flow than males, but this flow declines more rapidly with age in females.[69,72–74] The present study indicates that digital pathology methods may provide insights into structural changes that correlate with those physiological phenomena.

Conclusions

Though different antigens have been used as IHC markers for cerebral blood vessels in mice, few antibodies that we tested yielded a good combination of high signal and low background that was necessary for accurate detection and quantitation by digital pathology platforms. Of the markers that we tested, the best option was collagen IV IHC, which proved to be useful in both FFPE and free-floating sections, following technical optimization (see Supplementary Figure S1 for comparison of the staining workflows). Sections in both formats analyzed with the Aperio Microvessel Algorithm displayed high vessel recognition rates while minimizing the quantitation of either background or non-specific cell body staining, thus maximizing both

sensitivity and specificity. Subsequent exploratory analyses of immunostained FFPE sections showed sex- and region-specific differences in some of the calculated parameters, indicating that our methods can be applied for hypothesis testing, or hypothesis generation, in mouse models.

Declaration of conflicting interests

The author(s) declared no potential conflicts of interest with respect to the research, authorship, and/or publication of this article.

Authors' contributions

DN acquired, analyzed, and interpreted data and drafted and revised the manuscript. JG and EW acquired data and helped to revise the manuscript. PP acquired data and created artwork for the manuscript. DW, CN, and PN obtained funding, supplied the concepts for data acquisition, helped to revise the manuscript, and approved the version to be published.

Supplementary material

Supplemental material for this article is available online.

ORCID iD

Dana M Niedowicz 🔟 https://orcid.org/0000-0002-1052-898X

References

1. Bir SC, Khan MW, Javalkar V, et al. Emerging concepts in vascular dementia: a review. *J Stroke Cerebrovasc Dis* 2021; 30: 105864.
2. Caruso P, Signori R and Moretti R. Small vessel disease to subcortical dementia: a dynamic model, which interfaces aging, cholinergic dysregulation and the neurovascular unit. *Vasc Health Risk Manag* 2019; 15: 259–281.
3. Elahi FM, Wang MM and Meschia JF. Cerebral small vessel disease–related dementia: more questions than answers. *Stroke* 2023; 54: 648–660.
4. Kapasi A and Schneider JA. Vascular contributions to cognitive impairment, clinical Alzheimer's disease, and dementia in older persons. *Biochim Biophys Acta* 2016; 1862: 878–886.

5. Thal DR, Grinberg LT and Attems J. Vascular dementia: different forms of vessel disorders contribute to the development of dementia in the elderly brain. *Exp Gerontol* 2012; 47: 816–824.

6. Wardlaw JM, Smith C and Dichgans M. Small vessel disease: mechanisms and clinical implications. *Lancet Neurol* 2019; 18: 684–696.

7. Zanon Zotin MC, Sveikata L, Viswanathan A, et al. Cerebral small vessel disease and vascular cognitive impairment: from diagnosis to management. *Curr Opin Neurol* 2021; 34: 246–257.

8. Fisher RA, Miners JS and Love S. Pathological changes within the cerebral vasculature in Alzheimer's disease: new perspectives. *Brain Pathol* 2022; 32: e13061.

9. Quick S, Moss J, Rajani RM, et al. A vessel for change: endothelial dysfunction in cerebral small vessel disease. *Trends Neurosci* 2021; 44: 289–305.

10. Fisher DW, Bennett DA and Dong H. Sexual dimorphism in predisposition to Alzheimer's disease. *Neurobiol Aging* 2018; 70: 308–324.

11. Nedungadi TP and Clegg DJ. Sexual dimorphism in body fat distribution and risk for cardiovascular diseases. *J Cardiovasc Transl Res* 2009; 2: 321–327.

12. Sampathkumar NK, Bravo JI, Chen Y, et al. Widespread sex dimorphism in aging and age-related diseases. *Hum Genet* 2020; 139: 333–356.

13. Zalewska T, Pawelec P, Ziabska K, et al. Sexual dimorphism in neurodegenerative diseases and in brain ischemia. *Biomolecules* 2022; 13: 26.

14. Böhm B, Hartmann K, Buck M, et al. Sex differences of carotid intima-media thickness in healthy children and adolescents. *Atherosclerosis* 2009; 206: 458–463.

15. Connelly PJ, Casey H, Montezano AC, et al. Sex steroids receptors, hypertension, and vascular ageing. *J Hum Hypertens* 2022; 36: 120–125.

16. Moreau KL. Modulatory influence of sex hormones on vascular aging. *Am J Physiol Heart Circ Physiol* 2019; 316: H522–H526.

17. Seeland U, Nemcsik J, Lønnebakken MT, Sex and Gender VascAgeNet Expert Group, et al. Sex and gender aspects in vascular ageing – focus on epidemiology, pathophysiology, and outcomes. *Heart Lung Circ* 2021; 30: 1637–1646.

18. Torres-Espin A, Rabadaugh H, Fitzsimons S, et al. Sexually dimorphic differences in angiogenesis markers predict brain aging trajectories. *bioRxiv* 2023; 2023: 07.16.549192.

19. Ward JM and Rehg JE. Rodent immunohistochemistry: pitfalls and troubleshooting. *Vet Pathol* 2014; 51: 88–101.

20. Buglioni A, Guo R, Rumilla KM, et al. An unexpected diagnosis uncovered by quantitative molecular findings: a case report. *J Natl Compr Canc Netw* 2023; 21: 787–791.

21. Plass M, Kargl M, Kiehl TR, et al. Explainability and causability in digital pathology. *J Pathol Clin Res* 2023; 9: 251–260.

22. Neltner JH, Abner EL, Baker S, et al. Arteriolosclerosis that affects multiple brain regions is linked to hippocampal sclerosis of ageing. *Brain* 2014; 137: 255–267.

23. Aeffner F, Zarella MD, Buchbinder N, et al. Introduction to digital image analysis in whole-slide imaging: a white paper from the digital pathology association. *J Pathol Inform* 2019; 10: 9.

24. Hanna MG and Ardon O. Digital pathology systems enabling quality patient care. *Genes Chromosomes Cancer* 2023; 62: 685–697.

25. Scalco R, Hamsafar Y, White CL, et al. The status of digital pathology and associated infrastructure within alzheimer's disease centers. *J Neuropathol Exp Neurol* 2023; 82: 202–211.

26. Davri A, Birbas E, Kanavos T, et al. Deep learning for lung cancer diagnosis, prognosis and prediction using histological and cytological images: a systematic review. *Cancers* 2023; 15: 15.

27. Fu X, Sahai E and Wilkins A. Application of digital pathology-based advanced analytics of tumour microenvironment organisation to predict prognosis and therapeutic response. *J Pathol* 2023; 260: 578–591.

28. Rabilloud N, Allaume P, Acosta O, et al. Deep learning methodologies applied to digital pathology in prostate cancer: a systematic review. *Diagnostics (Basel, Switzerland)* 2023; 13: 13.

29. Fakhrejahani E, Asao Y and Toi M. Tumor microvasculature characteristics studied by image analysis: histologically-driven angiogenic profile. *Int J Biol Markers* 2014; 29: e204–7.

30. Konda VJ, Hart J, Lin S, et al. Evaluation of microvascular density in Barrett's associated neoplasia. *Mod Pathol* 2013; 26: 125–130.

31. Nam S, Chong Y, Jung CK, et al. Introduction to digital pathology and computer-aided pathology. *J Pathol Transl Med* 2020; 54: 125–134.

32. Salvi M, Michielli N and Molinari F. Stain color adaptive normalization (SCAN) algorithm: separation and standardization of histological stains in digital pathology. *Comput Methods Programs Biomed* 2020; 193: 105506.

33. Percie Du Sert N, Hurst V, Ahluwalia A, et al. The ARRIVE guidelines 2.0: updated guidelines for reporting animal research. *J Cereb Blood Flow Metab* 2020; 40: 1769–1777.

34. Belmaati Cherkaoui M, Vacca O, Izabelle C, et al. Dp71 contribution to the molecular scaffold anchoring aquaporine-4 channels in brain macroglial cells. *Glia* 2021; 69: 954–970.

35. Fujimoto T, Yaoi T, Nakano K, et al. Generation of dystrophin short product-specific tag-insertion mouse: distinct Dp71 glycoprotein complexes at inhibitory postsynapse and glia limitans. *Cell Mol Life Sci* 2022; 79: 109.

36. Sudduth TL, Weekman EM, Price BR, et al. Time-course of glial changes in the hyperhomocysteinemia model of vascular cognitive impairment and dementia (VCID). *Neuroscience* 2017; 341: 42–51.

37. Milosevic V, Edelmann RJ, Winge I, et al. Vessel size as a marker of survival in estrogen receptor positive breast cancer. *Breast Cancer Res Treat* 2023; 200: 293–304.

38. Krenacs L, Krenacs T, Stelkovics E, et al. Heat-Induced antigen retrieval for immunohistochemical reactions in routinely processed paraffin sections. In: Oliver C and

Jamur MC (eds.). *Immunocytochemical methods and protocols*. Totowa, NJ: Humana Press, 2010. p. 103–119.

39. Scalia CR, Boi G, Bolognesi MM, et al. Antigen masking during fixation and embedding, dissected. *J Histochem Cytochem* 2017; 65: 5–20.

40. Werner M, Chott A, Fabiano A, et al. Effect of formalin tissue fixation and processing on immunohistochemistry. *Am J Surg Pathol* 2000; 24: 1016–1019.

41. Levin M. A novel immunohistochemical method for evaluation of antibody specificity and detection of labile targets in biological tissue. *J Biochem Biophys Methods* 2004; 58: 85–96.

42. Vassilakopoulou M, Parisi F, Siddiqui S, et al. Preanalytical variables and phosphoepitope expression in FFPE tissue: quantitative epitope assessment after variable cold ischemic time. *Lab Invest* 2015; 95: 334–341.

43. Challa VR, Thore CR, Moody DM, et al. Increase of white matter string vessels in alzheimer's disease. *J Alzheimers Dis* 2004; 6: 379–383. discussion 443-9.

44. Miller VM, Kalaria RN, Hall R, et al. Medullary microvessel degeneration in multiple system atrophy. *Neurobiol Dis* 2007; 26: 615–622.

45. Mott RT, Thore CR, Moody DM, et al. Reduced ratio of afferent to total vascular density in mesial temporal sclerosis. *J Neuropathol Exp Neurol* 2009; 68: 1147–1154.

46. Batzdorf CS, Morr AS, Bertalan G, et al. Dimorphism in extracellular matrix composition and viscoelasticity of the healthy and inflamed mouse brain. *Biology* 2022; 11: 11.

47. Zhao J, Chen J, Li YY, et al. Bruton's tyrosine kinase regulates macrophage−induced inflammation in the diabetic kidney via NLRP3 inflammasome activation. *Int J Mol Med* 2021; 48: 177.

48. Franciosi S, De Gasperi R, Dickstein DL, et al. Pepsin pretreatment allows collagen IV immunostaining of blood vessels in adult mouse brain. *J Neurosci Methods* 2007; 163: 76–82.

49. Franciosi S, Gama Sosa MA, English DF, et al. Novel cerebrovascular pathology in mice fed a high cholesterol diet. *Mol Neurodegener* 2009; 4: 42.

50. Choi WJ, Li Y, Wang RK, et al. Automated counting of cerebral penetrating vessels using optical coherence tomography images of a mouse brain in vivo. *Med Phys* 2022; 49: 5225–5235.

51. Deán-Ben XL, Robin J, Nozdriukhin D, et al. Deep optoacoustic localization microangiography of ischemic stroke in mice. *Nat Commun* 2023; 14: 3584.

52. Pian Q, Alfadhel M, Tang J, et al. Cortical microvascular blood flow velocity mapping by combining dynamic light scattering optical coherence tomography and two-photon microscopy. *J Biomed Opt* 2023; 28: 076003.

53. Sargent SM, Bonney SK, Li Y, et al. Endothelial structure contributes to heterogeneity in brain capillary diameter. *Vascular Biology (Bristol, England)* 2023; 5

54. Wälchli T, Bisschop J, Miettinen A, et al. Hierarchical imaging and computational analysis of three-dimensional vascular network architecture in the entire postnatal and adult mouse brain. *Nat Protoc* 2021; 16: 4564–4610.

55. Ye D, Chen S, Liu Y, et al. Mechanically manipulating glymphatic transport by ultrasound combined with microbubbles. *Proc Natl Acad Sci U S A* 2023; 120: e2212933120.

56. Yu F, Wang F, Li K, et al. Real-time X-ray imaging of mouse cerebral microvessels in vivo using a pixel temporal averaging method. *J Synchrotron Radiat* 2022; 29: 239–246.

57. Boruah D, Deb P, Srinivas V, et al. Morphometric study of nuclei and microvessels in gliomas and its correlation with grades. *Microvasc Res* 2014; 93: 52–61.

58. Ley EJ, Scehnet J, Park R, et al. The in vivo effect of propranolol on cerebral perfusion and hypoxia after traumatic brain injury. *J Trauma* 2009; 66: 154–159. discussion 9-61.

59. Muellner A, Benz M, Kloss CU, et al. Microvascular basal lamina antigen loss after traumatic brain injury in the rat. *J Neurotrauma* 2003; 20: 745–754.

60. Di Ieva A, Bruner E, Widhalm G, et al. Computer-assisted and fractal-based morphometric assessment of microvascularity in histological specimens of gliomas. *Sci Rep* 2012; 2: 429.

61. Chen C, He ZC, Shi Y, et al. Microvascular fractal dimension predicts prognosis and response to chemotherapy in glioblastoma: an automatic image analysis study. *Lab Invest* 2018; 98: 924–934.

62. Bouras C, Kovari E, Herrmann FR, et al. Stereologic analysis of microvascular morphology in the elderly: Alzheimer disease pathology and cognitive status. *J Neuropathol Exp Neurol* 2006; 65: 235–244.

63. Kolinko Y, Marsalova L, Pena SP, et al. Stereological changes in microvascular parameters in hippocampus of a transgenic rat model of Alzheimer's disease. *J Alzheimers Dis* 2021; 84: 249–260.

64. Richard E, van Gool WA, Hoozemans JJM, et al. Morphometric changes in the cortical microvascular network in Alzheimer's disease. *J Alzheimers Dis* 2010; 22: 811–818.

65. Mozumder M, Pozo JM, Coelho S, et al. Quantitative histomorphometry of capillary microstructure in deep white matter. *NeuroImage-Clin* 2019; 23: 8.

66. Freitas-Andrade M, Comin CH, da Silva MV, et al. Unbiased analysis of mouse brain endothelial networks from two- or three-dimensional fluorescence images. *Neurophotonics* 2022; 9: 031916.

67. Tretiakova M, Antic T, Binder D, et al. Microvessel density is not increased in prostate cancer: digital imaging of routine sections and tissue microarrays. *Hum Pathol* 2013; 44: 495–502.

68. Deb P, Boruah D and Dutta V. Morphometric study of microvessels in primary CNS tumors and its correlation with tumor types and grade. *Microvasc Res* 2012; 84: 34–43.

69. Alisch JSR, Khattar N, Kim RW, et al. Sex and age-related differences in cerebral blood flow investigated using pseudo-continuous arterial spin labeling magnetic resonance imaging. *Aging (Albany NY)* 2021; 13: 4911–4925.

70. Connelly PJ, Jandeleit-Dahm KA and Delles C. Sex and gender aspects in vascular pathophysiology. *Clin Sci (Lond)* 2020; 134: 2203–2207.

71. Tang T, Hu L, Liu Y, et al. Sex-Associated differences in neurovascular dysfunction during ischemic stroke. *Front Mol Neurosci* 2022; 15: 860959.

72. Alwatban MR, Aaron SE, Kaufman CS, et al. Effects of age and sex on middle cerebral artery blood velocity and flow pulsatility index across the adult lifespan. *J Appl Physiol* 2021; 130: 1675–1683.

73. Pabbidi MR, Kuppusamy M, Didion SP, et al. Sex differences in the vascular function and related mechanisms: role of 17β-estradiol. *Am J Physiol Heart Circ Physiol* 2018; 315: H1499–H1518.

74. Rodriguez G, Warkentin S, Risberg J, et al. Sex differences in regional cerebral blood flow. *J Cereb Blood Flow Metab* 1988; 8: 783–789.